HHS Public Access

Author manuscript

Neurobiol Dis. Author manuscript; available in PMC 2018 July 01.

Published in final edited form as:

Neurobiol Dis. 2018 July ; 115: 182–193. doi:10.1016/j.nbd.2018.04.010.

Modulating membrane fluidity corrects Batten disease phenotypes *in vitro* and *in vivo*

Mark L. Schultz[a,1], **Luis Tecedor**[b,1], **Elena Lysenko**[b], **Shyam Ramachandran**[b], **Colleen S. Stein**[a], **Beverly L. Davidson**[b,c,*,1]

[a]Department of Internal Medicine, University of Iowa, Iowa City, IA 52242, United States

[b]The Raymond G. Perelman Center for Cellular and Molecular Therapeutics, The Children's Hospital of Philadelphia, Philadelphia, PA 19104, United States

[c]Department of Pathology & Laboratory Medicine, Philadelphia, PA 19104, United States

Abstract

The neuronal ceroid lipofuscinoses are a class of inherited neurodegenerative diseases characterized by the accumulation of autofluorescent storage material. The most common neuronal ceroid lipofuscinosis has juvenile onset with rapid onset blindness and progressive degeneration of cognitive processes. The juvenile form is caused by mutations in the *CLN3* gene, which encodes the protein CLN3. While mouse models of Cln3 deficiency show mild disease phenotypes, it is apparent from patient tissue- and cell-based studies that its loss impacts many cellular processes. Using Cln3 deficient mice, we previously described defects in mouse brain endothelial cells and blood-brain barrier (BBB) permeability. Here we expand on this to other components of the BBB and show that Cln3 deficient mice have increased astrocyte endfeet area. Interestingly, this phenotype is corrected by treatment with a commonly used GAP junction inhibitor, carbenoxolone (CBX). In addition to its action on GAP junctions, CBX has also been proposed to alter lipid microdomains. In this work, we show that CBX modifies lipid microdomains and corrects membrane fluidity alterations in Cln3 deficient endothelial cells, which in turn improves defects in endocytosis, caveolin-1 distribution at the plasma membrane, and Cdc42 activity. In further work using the NIH Library of Integrated Network-based Cellular Signatures (LINCS), we discovered other small molecules whose impact was similar to CBX in that they improved Cln3-deficient cell phenotypes. Moreover, Cln3 deficient mice treated orally with CBX exhibited recovery of impaired BBB responses and reduced auto-fluorescence. CBX and the compounds identified by LINCS, many of which have been used in humans or approved for other indications, may find therapeutic benefit in children suffering from CLN3 deficiency through mechanisms independent of their original intended use.

*Corresponding author at: 5060 Colket Translational Research Building, The Children's Hospital of Philadelphia, Philadelphia, PA 19104, United States. davidsonbl@email.chop.edu (B.L. Davidson).

[1]Denotes equal contribution.

Conflicts of interest

The data in this scientific report was used for patent application US14/776,558.

Data statement

All data is available upon request.

Keywords

Neuronal ceroid lipofuscinoses; JNCL; CLN3; Cav-1; Cdc42; Blood-brain barrier; Carbenoxolone; Membrane fluidity

1. Introduction

The neuronal ceroid lipofuscinoses (NCLs) are progressive neuro-degenerative diseases characterized by the accumulation of auto-fluorescent material in multiple cell types. The most common NCL has a juvenile onset and is commonly caused by mutations in *CLN3* (referred to as CLN3 deficiency) (Williams and Mole, 2012). CLN3 deficiency generally manifests with early visual deficits followed several years later by seizures with mental and physical decline (Phillips et al., 2005). To date, only palliative care is available for this invariably fatal disease.

The *CLN3* gene encodes the protein CLN3 (also known as battenin), which is a 438 amino acid hydrophobic, multi-pass transmembrane protein of unresolved function (Cotman and Staropoli, 2012; Phillips et al., 2005). Work in model systems over the last two decades suggest that CLN3 impacts multiple cellular functions including lysosomal pH (Golabek et al., 2000; Holopainen et al., 2001; Pearce et al., 1999; Pearce and Sherman, 1998), vesicular trafficking (Cao et al., 2006; Codlin and Mole, 2009; Fossale et al., 2004; Kama et al., 2011; Metcalf et al., 2008), palmitoyl desaturase activity (Narayan et al., 2006), endocytosis (Codlin et al., 2008; Fossale et al., 2004; Luiro et al., 2001; Luiro et al., 2004; Schultz et al., 2014; Tecedor et al., 2013; Vidal-Donet et al., 2013), and membrane microdomain formation or stability (Tecedor et al., 2013).

Using a *Cln3* reporter mouse we previously showed that *Cln3* is highly expressed in brain vasculature endothelial cells (Eliason et al., 2007). Brain endothelial cells are a component of the blood-brain barrier (BBB) and are vital for the maintenance of neuronal health and CNS function. In some neurodegenerative diseases, such as Alzheimer's disease, endothelial cell dysfunction (Sagare et al., 2013) at the BBB is a critical element in disease pathogenesis. Intriguingly, CLN3 disease patients and mouse models display autoantibodies against CNS antigens in peripheral blood. Concurrently, high levels of storage material accumulate in endothelial cells (Lamb et al., 2006; Lim et al., 2007). Additionally, *Cln3*-null mice have abnormal BBB responses to hypotonic stress *in vivo* (Tecedor et al., 2013). Whether other components of the BBB, for example astrocytes whose endfeet are a constituent of the BBB, are affected in CLN3 deficiency is not known.

Here, we report that *Cln3*-null mice have increased astrocyte endfeet area in the BBB. Increased astrocyte endfeet size could reflect defects in astrocyte communication, which occurs at GAP junctions. Indeed prior work in slice culture models have shown excessive astrocytic GAP junction connectivity (Burkovetskaya et al., 2014). Interestingly, we found that oral treatment of $Cln3^{-/-}$ mice with the GAP junction inhibitor Carbenoxolone (CBX) significantly corrects astrocyte endfeet area. CBX exerts its impact on GAP junction/hemichannel activity upon intercalation into the plasma membrane, which likely alters membrane microfluidity (Davidson and Baumgarten, 1988; Goldberg et al., 1996; Tovar

et al., 2009). Interestingly, we previously described altered plasma membrane fluidity in endothelial cells derived from *Cln3*$^{-/-}$ mice (Tecedor et al., 2013).

We next tested the hypothesis that CBX improves Cln3 phenotypes *in vitro* and *in vivo* by improving membrane fluidity defects. Our results show that, *in vitro*, CBX corrects previously reported lipid microdomain changes, caveolar and fluid phase endocytosis defects, and other downstream cellular pathologies reported in *Cln3*$^{-/-}$ mice cells including altered Cdc42-GTP levels. *In vivo*, CBX corrected altered BBB responses in *Cln3* deficient mice in addition to improving astrocyte endfeet phenotypes. Also, we took advantage of the NIH Library of Integrated Network-based Cellular Signatures (LINCS) database to identify other compounds that behave similarly to CBX in model systems. Overall our data present evidence supporting further testing of 7 compounds for potential treatment for CLN3 deficiency.

2. Materials and methods

2.1. Mice

All animal experiments were approved by the University of Iowa animal care and use committee and conducted in accordance with institutional and federal guidelines. Here we used WT, *Cln3*$^{lacZ/+}$ (*Cln3*$^{-/+}$), and *Cln3*$^{lacZ/lacZ}$ (*Cln3*$^{-/-}$) mice (Eliason et al., 2007) backcrossed to the C57BL/6J background. Mixes of male and female mice were used for experiments.

2.2. MBEC cell lines

Due to the low yield of primary MBECs, we used previously described immortalized MBEC from *Cln3*$^{-/-}$ mice (Tecedor et al., 2013). *Cln3* expression was stably restored in *Cln3*$^{-/-}$ MBEC using a lentivirus vector as described previously (Tecedor et al., 2013), creating the *Cln3*^{R}, sister cell line. *Cln3*^{R} and *Cln3*$^{-/-}$ MBECs behave similarly to primary wildtype and *Cln3*$^{-/-}$ MBECs (Schultz et al., 2014; Tecedor et al., 2013). Immortalized MBECs are positive for Von Willebrand factor and ZO-1 (Tecedor et al., 2013).

2.3. FRAP

2.3.1. Membrane fluidity—Cells were incubated with Alexa 488-CTB (Invitrogen) in the dark for 30 min on ice. Cells were briefly rinsed with ice-cold media and placed on ice in the dark until use. Imaging and photobleaching were conducted on a Zeiss LSM510 microscope (Carl Zeiss) equipped with an Ar 488 nm laser. 60 iterations at 100% of 488 nm excitation was used to photobleach a small portion (31 px diameter) of the membrane. Adjacent non photobleached membrane areas of the same size were used as a control for sequential bleaching as previously described (Tecedor et al., 2013).

2.3.2. GAP junction connectivity—MBECs were incubated with 5 μM calcein-AM (Molecular probes) for 30 min at 37 °C in the dark, then rinsed briefly with cold cell culture media. Whole cells were photobleached as described above in the *Membrane fluidity* section. Post-bleached images were captured every 5 s. Neighboring cells were used as controls for sequential bleaching due to the imaging process. FRAP was quantified as

described previously (Kenworthy, 2007). Results from three independent experiments were analyzed together (n = 76, 42, 52, 52 for *Cln3*$^{-/-}$, *Cln3*^{R}, *Cln3*$^{-/-}$+CBX, *Cln3*^{R}+CBX respectively). Two-way ANOVA resulted with significant interaction. Data was analyzed for each time point by one-way ANOVA followed by Tukey's post-hoc analysis.

2.4. Cholesterol quantification

Detergent-free carbonate extraction and discontinuous sucrose density centrifugation was used to enrich plasma membrane and separate lipid microdomain fractions as before (Tecedor et al., 2013). Cholesterol was quantified by amplex red assay (Life Technologies). Briefly, cell fractions were diluted in reaction buffer and incubated with the amplex red reagent per the manufactures instructions. Cholesterol intensity was quantified for each membrane fraction with a monochrome microplate reader Safire2 (Tecan Group Ltd. Mannedorf, Switzerland). Results were normalized to total amount of quantified cholesterol per the manufacturer's instructions.

2.5. Cdc42-GTP analysis

The Cdc42 G-Lisa® from Cytoskeleton Inc. was utilized for measurement of Cdc42-GTP levels. Briefly, 0.8 mg/ml of snap frozen lysate was incubated in the ELISA plate and the manufactures instructions were followed for detection and analysis as previously described (Schultz et al., 2014). Data were normalized to the protein standard and significance was tested by one-way ANOVA with Tukey post-hoc analysis.

2.6. Fluid-phase endocytosis

Subconfluent cells were incubated with 0.5 mg/ml Alexa 488 10,000 MW dextran (Invitrogen) for 20 min. Then cells were briefly washed 3× with 37°C PBS to remove unbound dextran and immediately fixed with 4% PFA at 37 °C. Membrane impermeable 200 mM Red-40 was added to quench extra cellular dextran signal allowing quantification of only internalized dextran (Schultz et al., 2014). Cells were immediately imaged on an Olympus IX81 microscope and fluorescent intensity was calculated by ImageJ. Significance was determined by a one-way ANOVA with Tukey post-hoc (Fig. 5C) analysis or one-way ANOVA with Holm-Sidak's multiple comparisons post-hoc (Fig. 6B) comparing each treatment with the Cln3$^{-/-}$ MBEC + vehicle group.

2.7. Scratch assay

MBECs were grown to confluence and a pipette tip was used to create a wound. Cells were briefly washed with PBS and cell culture media was added for the remainder of the experiment. Cells were imaged every hour on an automated live cell Olympus IX81 microscope overnight. T-Scratch software (Geback et al., 2009) was used to quantify wound closure. Significance was assessed by 2-way ANOVA with Bonferroni post-hoc test (Schultz et al., 2014).

2.8. Immunofluorescence

Sub-confluent MBECs were briefly washed and fixed in 4% PFA, permeabilized with 0.01% Trition-X-100, washed three times with PBS, and blocked for 1 h with 10% goat serum.

Cells were incubated overnight with Cav-1 antibody (1:200) Abcam, washed three times, and incubated with goat anti-rabbit Alexa 488 secondary for 45 min in the dark. After mounting with Vectashield, cells were imaged on a Zeiss 710 confocal microscope.

2.9. Protein analysis

Three confluent 160-mm-diameter dishes of MBECs were harvested and plasma membranes were isolated as previously described (Yao et al., 2009). Protein concentrations were determined by Bio-Rad Dc-Protein assay (Bio-Rad). Samples were mixed with Bio-Rad XT sample buffer and reducing agent, run on Criterion™ XT 4–12% Bis-Tris Gels (Bio-Rad), and transferred onto PVDF membranes. Immunodetection was performed with (1:100) rabbit anti-connexin 43 antibody (Invitrogen), (1:500) mouse anti phospho-caveolin1 (pY14) (BD Transduction Laboratories), (1:5000) rabbit anti-β-catenin (Abcam), (1:1000) rabbit anti-Cav-1 (Abcam), or (1:1000) mouse-anti-transferrin receptor (Life Technology) followed by HRP-coupled secondary antibodies (Jackson ImmunoResearch), and developed with ECL-Plus (GE Healthcare). Protein bands were quantified by densitometry using Image Lab 5.1 (Bio-Rad) software. Plasma membrane connexin43 levels were normalized to plasma membrane transferrin receptor. This value was normalized to total β-catenin as a housekeeping reference protein.

2.10. BBB hypotonic treatment

Mice were anesthetized and perfused with a Gilson minipulse *3* pump (set to a speed of 2). We sequentially perfused i) 175 μl Alexafluor 488 WGA (1 mg/ml) (preloaded into the needle); ii) Hoechst 33258 (100 μg/ml in 1 mM $CaCl_2$ hypotonic solution), injected for 2 min and 15 s; iii) saline, perfused for 30 s; iv) 4% PFA, perfused for 2 min. Each solution was passed through an IV drip tube to create continuous flow and pressure. After dissection and removal, brains were post-fixed in 4% PFA for 3 h, embedded in agar and set on ice to solidify. Solidified blocks were trimmed and further post-fixed in 4% PFA at 4 °C overnight. 50-μm vibratome sections were mounted onto slides, cover-slipped with Fluorogel and immediately imaged on a Leica Leitz DMRBE microscope or Zeiss LSM710 confocal microscope. Images were captured in the *green* (WGA), *blue* (Hoechst), and *red* (autofluorescence) channels and channels combined in Adobe Photoshop.

2.11. Astrocyte endfeet quantification

3 mice per group were perfused with 2.5% glutaraldehyde in 0.1 M sodium cacodylate buffer using a Gilson minipulse 3 at ~1.3 ml/min flow ratio for maintaining BBB integrity. Motor cortex samples of $1mm^2$ were collected, and 50 μm vibrotome sections were obtained. Samples were then postfixed in 1% osmium tetroxide for 1 h., stained with uranyl acetate, dehydrated in a graded ethanol series, and embedded in Epon resin. Ultrathin 70 nm sections were cut on a Leica UC6 ultra-microtome (Leica Microsystems) and 12–23 cortical capillaries per animal analyzed with a 1230 JEOL-JEM transmission EM (Jeol USA) or a Zeiss Libra 120 transmission EM. Microvasculature was recognized by detecting the basal lamina which is localized between endothelial cells and astrocytic endfeet. Only long processes surrounding the basal lamina were measured to exclude neuronal terminals. The area surrounded by astrocytic endfeet plasma membrane was measured using ImageJ software (NIH). Endfeet data did not follow a normal distribution so it was normalized

by lognormal transformation. Statistical significance of the normalized data was tested by two-tailed *t*-test.

2.12. Autofluorescence

Brains were collected as explained above in the BBB hypotonic treatment method. From each brain, 20 X images were taken from four different sections of medial cortex. Autofluorescence images were collected in the red channel and intensity calculated using ImageJ. Significance was calculated by a one-way ANOVA with Tukey post-hoc analysis.

2.13. Drug treatment

Carbenoxolone disodium salt (Abcam) was dissolved to 0.5 M in ethanol:water (1:1), and further diluted in cell culture media to obtain the following final concentrations and treatment durations: 50 μM for 2 h. (G-LISA), 25 μM for (30 min fluid-phase endocytosis; 2 h. FRAP, cholesterol, cav-1 trafficking), and 3 μM overnight (scratch assay). In the multidrug screening experiment, CBX was dissolved with DMSO and diluted in cell culture media to a final concentration of 3 μM for a 24 h. treatment. For *in vivo* experiments, a 30 mg/ml stock solution of carbenoxolone was prepared in saline (vehicle) and diluted to 2.0 mg/ml for gavage. Mice were administered 20 mg/kg CBX or vehicle by gavage, given at the same time each morning for 14 days.

Enoxenolone (Enx, Abcam) was dissolved in ethanol:water (1:1) and diluted in cell culture media to a final concentration of 3 μM.

Drugs tested in the multidrug screening test were dissolved in DMSO and then diluted in cell culture media for 24 h. treatment. Experimental concentrations matched those recommended on the LINCS database: Prednisolone (Prd, Sigma-Aldrich) and α-ketocholesterol (α-KC, Sigma-Aldrich) at 10 μM, BRD-K95814727 (K8, Broad Institute), -K30446755 (K4, Broad Institute), -K33258928 (K2, Broad Institute) at 5 μM, and BRD-K95985487 (K9, Broad Institute) at 0.5 μM.

2.14. LINCS database analyses

Cln3$^{-/-}$ MBE cells were treated with 3 μM CBX or no-treatment for 18 h., following which RNA was harvested from 6 wells per condition using the mirVana™ total RNA isolation kit procedure. Total RNA was tested for quality on an Agilent Model 2100 Bioanalyzer (Agilent Technologies), and gene expression profiles were generated using the MouseRef-8 V2 BeadChip Kit (Illumina).

Differential gene expression analysis was performed using the Partek® Genomics Suite®, Gene Expression workflow to identify the most significant up- and down-regulated genes. LINCS queries are based on a set of 1000 landmark genes which are representative of the whole transcriptome. To acquire the required number of genes we used a p value cutoff < 0.02 and > 1.2 gave roughly 200 genes in each category, which is required for reaching 150–200 up or down regulated landmark genes for the query. The fold changes of the genes were then uploaded onto the Apps.lincscloud.org/start (now https://clue.io/) to query the LINCS database.

Every reference signature in the database is compared with the query signatures and given a score termed the "connectivity score" based on the extent of similarity between the two. Scores range from +1 meaning higher similarity, to 0 meaning no similarity, to −1 meaning opposite similarity. We removed all non-compounds and negative connectivity scores, and sorted the remaining compounds by connectivity score alone. We prioritized the top 70 compounds with the highest connectivity score for further analysis.

2.15. Experimental design and statistical analysis

Data are presented as mean ± s.e.m. with *p* values, and sample size (n). Prism v6 (GraphPad Software) was used for statistical analyses. Comparisons between different datasets were made depending on data distribution tested by the D'Agostino normality test. Parametric tests were used for normally distributed data (two-tailed *t*-test for comparing two groups and ANOVA for comparing three or more groups). A two-way ANOVA was used to determine significance in experiments with multiple time points and groups. When a significant interaction was found between factors by two-way ANOVA, one-way ANOVA were used to determine significance between experimental groups. When the normality assumption was violated, nonparametric tests were performed (Mann-Whitney test for two groups and Kruskal-Wallis for three or more groups) unless the n was high enough to allow the transformation of the data to a normal distribution using lognormal function. Differences were considered statistically significant at $p < 0.05$. Different levels of significance between groups were denoted as * $p < 0.05$, ** $p < 0.01$, *** $p < 0.001$, **** $p < 0.0001$.

3. Results

3.1. An astrocyte endfeet phenotype in Cln3-null mice is corrected by CBX

At the BBB, astrocytes and brain endothelial cells are juxtaposed at astrocyte endfeet, which together serve to regulate BBB maintenance and function (Abbott et al., 2006). As we previously described structural alterations in mouse brain endothelia *in vivo* (Tecedor et al., 2013), we next tested cerebral sections for structural changes in *Cln3*$^{-/-}$ mice astrocytes. Transmission electron microscopy (TEM) analysis revealed astrocyte endfeet area in *Cln3*$^{-/-}$ mice was significantly increased at 0.2661 μm^2 (± 0.03003) compared to 0.0003332 μm^2 (± 0.02956) in *Cln3*$^{+/+}$ littermates (Fig. 1A). Given prior work showing impaired GAP junction connectivity in JNCL astrocytes (Burkovetskaya et al., 2014) we subsequently tested if treating *Cln3*$^{-/-}$ mice with the GAP junction inhibitor carbenoxolone (CBX) could impact this phenotype. CBX was administered daily to *Cln3*$^{-/-}$ mice or normal littermates for two weeks by oral gavage, and endfeet area assessed as before by TEM. CBX reduced astrocyte endfeet area in *Cln3*$^{-/-}$ mice to 0.1291 μm^2 (± 0.03120), which is similar to that found in control littermates (0.01833 ± 0.03310 μm^2; Fig. 1B).

3.2. CBX modifies microdomain fluidity

Gap junctions are produced by coupling the plasma membrane-resident hemichannels of adjacent cells allowing the exchange of cytoplasmic molecules and electrical signals. Due to the crosstalk between astrocytes and brain endothelial cells, we investigated *in vitro* GAP junction activity in brain endothelial cells derived from *Cln3*$^{-/-}$ mice. We used our previously established mouse brain endothelial cell lines (MBECs) for this work; this

includes a *Cln3*-null line (*Cln3*$^{-/-}$ MBECs), and a line in which *Cln3* expression was restored (*Cln3*^{R} MBECs). These cells behave similarly to primary MBECs from null or WT mice, respectively (Schultz et al., 2014; Tecedor et al., 2013). To study the impact of Cln3 deficiency on GAP junction connectivity, MBEC mono-layer cultures were incubated with calcein-AM, which moves between cells using GAP junctions and the cell-cell transfer rate quantified using whole cell fluorescence recovery after photobleaching (FRAP). For FRAP, the fluorescent calcein-AM in one cell is photobleached and then sequential images taken to determine the rate by which the dye enters the photobleached cell from neighboring cells. FRAP analysis revealed that *Cln3*$^{-/-}$ cells have a faster calcein-AM fluorescence recovery (one-way ANOVA, $F(3,112) = 30.22$, $p < 0.0001$) relative to *Cln3*^{R} cells, indicating increased flow of calcium-AM through GAP junctions with neighboring cells (Fig. 2A). As expected, treating cells with the reported GAP junction inhibitor CBX blunted the rate of fluorescence recovery in the photobleached cells (Fig. 2A). Connexin 43 (Cx43) levels, which is a main component of GAP junctions in the brain, were similar between *Cln3*$^{-/-}$ and *Cln3*^{R} MBECs (Fig. 2B; Kruskal-Wallis, $p = 0.1085$). This indicates that increased GAP junction activity is not caused by more Cx43 protein and suggests another mechanism for increased calcium-AM flow.

Although CBX is commonly used as a GAP junction inhibitor, data also support the notion that it directly modifies cell membranes. Administration of CBX to purified lysosomes stabilizes membranes (Porta et al., 1986; Symons et al., 1978), and incubation of enveloped viral particles with CBX reduces adsorption (Dargan and Subak-Sharpe, 1986) and viral release (Dargan and Subak-Sharpe, 1986). As GAP junctions are associated with cholesterol-rich domains (Schubert et al., 2002) and regulated by membrane fluidity (Bastiaanse et al., 1993), we tested if CBX influences lipid microdomain dynamics by evaluating GM1 ganglioside movement in the plasma membrane. GM1 gangliosides were labeled in living MBECs with Alexa-488-cholera toxin subunit B (A488-CTB) and a high intensity laser was used to photobleach a A488-CTB-positive region of the plasma membrane. Sequential images were captured to assess the rate of A488-CTB movement into the photobleached area. Consistent with our previous report (Tecedor et al., 2013), *Cln3*$^{-/-}$ MBECs displayed significantly faster recovery compared to *Cln3*^{R} cells, indicating enhanced membrane fluidity (Fig. 3A). When MBECs were tested after 2 h of CBX treatment, fluorescence recovery in *Cln3*$^{-/-}$ cells was normalized (one-way ANOVA $F(3,108) = 18.10$, $p < 0.0001$) (Fig. 3A).

To determine if CBX corrects the previously described abnormal distribution of microdomain lipids (Tecedor et al., 2013), plasma membranes were isolated and fractionated over sucrose gradients using a detergent-free extraction method and cholesterol levels quantified. Similar to our earlier data (Tecedor et al., 2013), *Cln3*$^{-/-}$ MBECs demonstrated cholesterol partitioning into more buoyant fractions, with the highest concentration found in the first (lightest) fraction compared to a cholesterol peak in the second fraction for *Cln3*^{R} MBEC (two-way ANOVA of “membrane fraction” factor $F(11,96) = 60.30$, $p < 0.0001$; Fig. 3B). Pretreatment with CBX normalized the profile of *Cln3*$^{-/-}$ MBECs such that cholesterol concentration peaked in fraction 2. (Fig. 3B, Fig. S1).

Cumulatively, these data support a model where CBX is a novel modifier of lipid microdomains. Interestingly, CBX did not significantly alter microdomain dynamics or the partitioning of cholesterol in *Cln3*^{R} MBECs.

3.3. CBX restores Cav-1 plasma membrane distribution

Since CBX corrected membrane fluidity dynamics in *Cln3*$^{-/-}$ MBECs, we subsequently investigated if CBX corrects caveolar defects. Caveolae are flask-shaped invaginations that form within distinct cholesterol/sphingolipid-enriched lipid microdomains on the plasma membrane. Caveolae are common in BBB endothelia, where they serve as signaling platforms, mediate endocytosis, and transcytosis. The primary structural protein of caveolae is caveolin-1 (Cav-1). Cav-1 inserts into membranes at the ER and traffics through the Golgi where high-order oligomerization drives transport to the plasma membrane (Chadda et al., 2007). We previously found enhanced microdomain fluidity in *Cln3*$^{-/-}$ MBECs and modified Cav-1 distribution as assessed by fractionation and immunofluorescence of the plasma membrane. Altered plasma membrane Cav-1 distribution causes reduced caveolae formation *in vitro* and *in vivo* (Tecedor et al., 2013). As shown in Fig. 4, CBX treatment of *Cln3*$^{-/-}$ MBECs increased Cav-1 immunosignal at the plasma membrane, evaluated by immunocytochemistry (Fig. 4A); western blot analysis of membrane enriched fractions showed no differences in Cav-1 protein levels (one-way ANOVA, $F(3,20) = 0.3744$, $p = 0.7724$; Fig. 4B) implying that trafficking not protein expression levels were impacted by CBX treatment. The corrective effect of CBX on these phenotypes is similar to our prior work where addition of exogenous lipids recovered Cav-1 plasma membrane localization (Tecedor et al., 2013). Cumulatively, the data support that CBX is acting to modify membranes in MBECs.

3.4. CBX corrects Cdc42-dependent defects in Cln3$^{-/-}$ MBECs

In addition to caveolar endocytosis, *Cln3*$^{-/-}$ MBECs have decreased levels of fluid-phase endocytosis (FPE) and increased GTP-loaded Cdc42 (Schultz et al., 2014). Cdc42 is a small GTPase that cycles between GTP-bound (active, effector-binding) and GDP-bound (inactive) states (Chadda et al., 2007; Nevins and Thurmond, 2006; Rojas et al., 2001). Cdc42 GTP-to-GDP cycling is required for fluid-phase endocytosis and cell migration, both of which are reduced in *Cln3*$^{-/-}$ cells (Schultz et al., 2014). This suggests that inefficient cycling of Cdc42 to the “off” state underlies multiple actin-related defects in MBEC, and suggests further that drugs able to promote cycling may have beneficial effects.

We incubated subconfluent MBECs with CBX and quantified Cdc42-GTP levels. As expected, in vehicle-treated cells, active Cdc42 levels were significantly higher in *Cln3*$^{-/-}$ compared to *Cln3*^{R} MBECs (Fig. 5A). In *Cln3*^{R} MBECs, CBX did not significantly alter Cdc42-GTP levels (Fig. 5A), likely due to the already low baseline levels of Cdc42-GTP as shown previously (Schultz et al., 2014). In contrast, CBX treatment significantly reduced the levels of Cdc42-GTP in *Cln3*$^{-/-}$ MBECs (Fig. 5A; ANOVA, $F(3, 16) = 9.947$, $p = 0.0006$).

Correction of Cdc42-GTP suggested that CBX may mitigate the downstream actin-dependent cell migration and fluid-phase endocytosis defects previously found in *Cln3*$^{-/-}$ cells (Schultz et al., 2014). To test for correction of cell migration, a scratch wound was

made in confluent monolayers of *Cln3*^{R} and *Cln3*$^{-/-}$ MBECs. Cells were subsequently treated with vehicle or CBX overnight and imaged using live cell microscopy to assess cell migration over time, and the percentage of wound remaining at each time point calculated. As in our former report (Schultz et al., 2014), *Cln3*^{R} MBECs migrated significantly faster than *Cln3*$^{-/-}$ cells at all-time points past 6 h (Fig. 5B). Importantly, CBX treatment improved *Cln3*$^{-/-}$ MBEC migration, such that there was no significant difference between *Cln3*^{R}, *Cln3*^{R} + CBX or *Cln3*$^{-/-}$ + CBX groups (Fig. 5B, Fig. S2). Thus, CBX is effective at correcting the cell migration defect in *Cln3*$^{-/-}$ MBECs.

In addition to the role of Cdc42 on cell migration, Cdc42 is a key regulator of fluid-phase endocytosis (Kumari and Mayor, 2008; Schultz et al., 2014). Impaired fluid phase endocytosis has been reported for *Cln3* mutant yeast, *Cln3*$^{-/-}$ mouse brain endothelial cells, *Cln3*$^{-/-}$ neuronal cells, and in fibroblasts harvested from patients with CLN3 deficiency (Codlin et al., 2008; Fossale et al., 2004; Luiro et al., 2004; Schultz et al., 2014; Vidal-Donet et al., 2013). We therefore measured fluid-phase endocytosis by uptake of fluorescently labeled dextran in cells treated with CBX or vehicle. CBX pretreatment of *Cln3*$^{-/-}$ MBECs for 30 min prior to dextran addition corrected *Cln3*$^{-/-}$ fluid-phase endocytic defects (Fig. 5C; (ANOVA, $F(3, 8) = 10.68$, $p < 0.0036$) to levels similar to *Cln3*^{R} cells. Together these results show that in *Cln3*$^{-/-}$ MBECs, CBX improves Cdc42 regulation and the associated actin-dependent functions. To our knowledge, the impact of CBX on Cdc42 activity and Cdc42-dependent cellular processes has not been previously tested.

3.5. LINCS compounds correct fluid-phase and caveolar defects in Cln3$^{-/-}$ MBECs

We next employed a transcriptome-based discovery approach to identify drugs that may mimic the effects of CBX (Fig. 6A). We generated gene expression signatures from *Cln3*$^{-/-}$ MBEC cells treated with 3 μM CBX *vs.* vehicle treated cells and normal cells. These signatures were used to mine the NIH Library of Integrated Network-based Cellular Signatures (LINCS) (Lamb et al., 2006) to identify small molecules that induced gene expression profiles similar to that induced by CBX. We also analyzed the effect of enoxolone, a metabolite of CBX (Iveson et al., 1971). Of hits, we focused on hydrophobic, neutral molecules that could impact membrane fluidity, and screened these for their ability to correct FITC-dextran uptake. The top six molecules (Prd, α-KC, K8, K9, K4, and K2) significantly increased fluid-phase endocytosis in *Cln3*$^{-/-}$ MBEC (Fig. 6B; one-way ANOVA, $F(9,128) = 15.58$, $p < 0.0001$), similar to CBX.

For caveolar endocytosis to occur, plasma membrane Cav-1 is phosphorylated. In *Cln3*$^{-/-}$ MBECs, the altered distribution of Cav-1 at the plasma membrane coincides with a decrease of caveolae number and reduction in phosphorylated Cav-1 (P-cav-1) (Tecedor et al., 2013). We therefore tested if plasma membrane-resident phospho-cav-1 was corrected by the LINCS hit compounds. Interestingly, we found that P-cav1 levels significantly recovered after treatment with CBX, its metabolite enoxolone, α-KC, K8, or K9 (Fig. 6C; Mann-Whitney test). Treatment with Prd, K4, or K2 did not reach statistical significance but showed a positive trend (Fig. 6C).

3.6. In vivo CBX treatment increases BBB responses and reduces autofluorescence

Brain endothelial cells are vital for maintaining the integrity of the BBB. Interestingly, injecting hypotonic solutions into blood induces an osmotic gradient across the BBB endothelium (Tecedor et al., 2013). In wildtype mice, this osmotic gradient triggers endothelial cell swelling followed by over-shrinkage, allowing small molecule access to the underlying neuropil (Kozler and Pokorny, 2003; Reid and O'Neil, 2000; Tecedor et al., 2013). The *in vivo* response to hypotonic shock is defective in *Cln3*$^{-/-}$ mice, as demonstrated by impaired passage of small molecule reporters into the brain (Tecedor et al., 2013). Here we tested if short-term oral dosing of CBX corrects this defect in aged (8-month old) *Cln3*-null mice. For this, *Cln3*$^{-/-}$ and *Cln3*$^{+/+}$ mice were gavaged daily with low-dose CBX or vehicle for two weeks, after which they were subjected to hypotonic challenge along with a dye that, unless the vasculature is compromised (*e.g.*, by hypotonic challenge), remains restricted to the vascular lumen. As before, we used Hoechst dye penetration as a readout for the leakiness of the vasculature (Tecedor et al., 2013). For optimal detection of dye leaking into brain parenchyma, our procedure was modified to include sequential delivery of i) labeled Alexa488-conjugated wheat germ agglutinin (WGA) to label the luminal surfaces of the vasculature, ii) isotonic (control) or hypotonic solution containing Hoechst dye, and iii) fixative (Fig. 7A). As expected, *Cln3*$^{+/+}$ mice treated with isotonic solution do not show extravasation of dye into the brain parenchyma but instead, the dye remains confined to the vessel lumen (Fig. 7A). In vehicle-gavaged mice, hypotonic-induced Hoechst penetration was evident in *Cln3*$^{+/+}$ mice, but minimal in *Cln3*$^{-/-}$ mice (Fig. 7B), in line with our previous report (Tecedor et al., 2013). In contrast, CBX-treated *Cln3*$^{-/-}$ mice had substantially increased Hoechst signal in the parenchymal tissue, with the amount of Hoechst dye penetration similar to *Cln3*$^{+/+}$ mice treated with CBX (Fig. 7B). These data indicate that CBX normalizes the impaired BBB response of *Cln3*$^{-/-}$ mice.

In addition to the various BBB defects, JNCL patients and *Cln3* mutant mouse models display progressive accumulation of auto-fluorescence in multiple cell types (Cotman et al., 2002; Mole et al., 2005; Stein et al., 2010). Due to the close proximity of the BBB to brain neuropil, we next investigated if CBX alters the accumulation of parenchymal autofluorescence. For this study, aged (8 month old) *Cln3*$^{+/+}$ and *Cln3*$^{-/-}$ mice were gavaged with CBX or vehicle for two weeks and cortical autofluorescence quantified. As expected, vehicle treated *Cln3*$^{-/-}$ mice showed extensive autofluorescence levels compared to wildtype mice. Of note, there was significant reduction of auto-fluorescence (Kruskal-Wallis, $p = 0.0234$) in CBX-treated *Cln3*$^{-/-}$ mice relative to those that received vehicle-treatment (Fig. 7C).

4. Discussion

We show that *Cln3*$^{-/-}$ mice have increased astrocytic endfeet area (Fig. 1A). Interestingly, enlarged astrocytic endfeet were lacking the notable organelles or membrane inclusions typically seen in these structures. Astrocyte endfeet swelling is an indicator of BBB dysfunction and is commonly found in stroke (Xiang et al., 2016). Post stroke, astrocyte endfeet swelling is hypothesized to prevent serum protein entry into the brain (Xiang et al., 2016). Enlarged astrocyte endfeet in *Cln3*$^{-/-}$ deficient mice may explain the decreased

permeability of the Hoechst dye into the brain during hypotonic stress (Fig. 7). Interestingly, this phenotype improved with CBX treatment (Fig. 1B).

Additionally, we found increased GAP junction activity in MBECs which was corrected with CBX (Fig. 2). Although CBX is a GAP junction inhibitor, our data support that it also modifies lipid microdomains, affecting fluidity and correcting the regulation and function of caveolar and fluid-phase endocytosis (Figs. 2–5). CBX is hypothesized to alter hemi channel opening or synaptic transmission by directly intercalating into the plasma membrane (Davidson and Baumgarten, 1988; Goldberg et al., 1996; Tovar et al., 2009). This is consistent with previous reports where CBX was shown to have membrane stabilizing effects, which are dependent on lipid concentration (Symons and Parke, 1980). Interestingly, CBX application to wild type cells had little effect, suggesting that the microdomain modifying effect of CBX may be context dependent.

Although we demonstrate an effect on membrane dynamics, the exact mechanism of how CBX modifies lipid microdomains or corrects the *in vitro* and *in vivo* phenotypes tested here is not known. CBX can modify lysosomal permeability (Symons and Parke, 1980), reduce fatty acid induced reactive oxygen species, inhibit sterol regulatory element binding protein-1c (Rhee et al., 2012), alter calcium signaling (Liu et al., 2010), inhibit 11-beta hydroxysteroid dehydrogenase (Monder et al., 1989), and increase heat shock protein expression (Nagayama et al., 2001). One could argue that modulation of one or more of these pathways could influence the cellular phenotypes investigated in this study. However, we found that CBX restores most *in vitro* cell phenotypes quickly (within 1–2 h), and speculate that it has a direct influence on cell membranes, creating conformational shifts and altered functions of membrane-associated proteins.

We also found other small molecules that behaved similarly to CBX (Fig. 6). These were identified using an unbiased genomics-based drug-discovery strategy (NIH Library of Integrated Network-based Cellular Signatures, LINCS). Compound screening allowed us to prioritize six small molecules that rescued membrane dynamics to levels comparable to CBX. Interestingly, all six small drugs are uncharged and hydrophobic. These drugs have the potential to intercalate into membranes and produce physicochemical effects on lipid bilayers (Royer et al. 2009, Ragot et al. 2013, Heier et al. 2013). These drugs were effective at correcting fluid-phase endocytosis and Cav-phosphorylation in *Cln3*$^{-/-}$ cells, and support the hypothesis that correcting membrane deficiencies in JNCL may be therapeutically beneficial (Fig. 6).

CXB has a steroid-like structure and a blood half-life of 13–26 h (Baron et al., 1978; Davidson and Baumgarten, 1988; Hayes et al., 1977). Recently a BBB-permeable derivative of CBX (Leshchenko et al., 2006), INI-0602, was used to alleviate excessive hemichannel activity associated with *Cln3*$^{-/-}$ mouse glial cells, and this drug showed positive effects in *Cln3*$^{-/-}$ mouse slice culture models (*Burkovetskaya* et al., 2014). Using a novel BBB permeability assay, we found that CBX treatment restored the BBB response to hypotonic shock. Moreover, two-weeks of CBX treatment resolved autofluorescence in *Cln3*$^{-/-}$ mouse brain (Fig. 7).

Rodent gut microflora hydrolyzes CBX into sulfate conjugates of enoxolone (Iveson et al., 1971), which enters the blood stream with subsequent presence in the brain and CSF (Tabuchi et al., 2012). Interestingly, both CBX, and enoxolone corrected the *in vitro* phenotypes. As CBX does not cross the BBB (Leshchenko et al., 2006; Takeuchi et al., 2011), the metabolite enoxolone may be responsible for the reduced autofluorescent storage either by improving the astrocytic phenotype, the endothelial phenotype, or both. Studies show that amyloid-β accumulation in Alzheimer's disease brain is due in part to faulty clearance by brain endothelial cells (Sagare et al., 2013), and recent work in the JNCL field shows that, *in vitro*, normalizing astrocytes can improve neuronal phenotypes (Parviainen et al., 2017). Regardless of the exact cell type and mechanism of action, CBX and the LINCS compounds provide promising therapeutic avenues for treatment of CLN3 deficiency disease.

Supplementary Material

Refer to Web version on PubMed Central for supplementary material.

Acknowledgments

This work was supported by: Beyond Batten Disease Foundation Fellowship, BDSRA Fellowship, the Roy J. Carver Trust, the UI Central Microscopy and Research Facility (1S10RR025439-01) and the Children's Hospital of Philadelphia Research Institute. We thank the Bioimaging Center at the Delaware Biotechnology Institute for access to their Zeiss Libra 120 transmission EM (supported by grants from the NIH-NIGMs (P20 GM103446), the NSF (IIA-1301765) and the State of Delaware). The funding bodies were not involved in study design, data collection and analysis, writing, or decision to submit the article for publication.

Appendix A. Supplementary data

Supplementary data to this article can be found online at https://doi.org/10.1016/j.nbd.2018.04.010.

References

Abbott NJ, et al. 2006; Astrocyte-endothelial interactions at the blood-brain barrier. Nat Rev Neurosci. 7 :41–53. [PubMed: 16371949]

Baron JH, et al. 1978; Serum carbenoxolone in patients with gastric and duodenal ulcer: absorption, efficacy and side-effects. Gut. 19 :330–335. [PubMed: 648939]

Bastiaanse EM, et al. 1993; Heptanol-induced decrease in cardiac gap junctional conductance is mediated by a decrease in the fluidity of membranous cholesterol-rich domains. J Membr Biol. 136 :135–145. [PubMed: 7508980]

Burkovetskaya M, et al. 2014; Evidence for aberrant astrocyte Hemichannel activity in juvenile neuronal ceroid Lipofuscinosis (JNCL). PLoS One. 9 :e95023. [PubMed: 24736558]

Cao Y, et al. 2006; Autophagy is disrupted in a knock-in mouse model of juvenile neuronal ceroid lipofuscinosis. J Biol Chem. 281 :20483–20493. [PubMed: 16714284]

Chadda R, et al. 2007; Cholesterol-sensitive Cdc42 activation regulates actin poly-merization for endocytosis via the GEEC pathway. Traffic. 8 :702–717. [PubMed: 17461795]

Codlin S, Mole SE. 2009; *S. pombe* btn1, the orthologue of the Batten disease gene CLN3, is required for vacuole protein sorting of Cpy1p and Golgi exit of Vps10p. J Cell Sci. 122 :1163–1173. [PubMed: 19299465]

Codlin S, et al. 2008; btn1 affects endocytosis, polarization of sterol-rich membrane domains and polarized growth in *Schizosaccharomyces pombe*. Traffic. 9 :936–950. [PubMed: 18346214]

Cotman SL, Staropoli JF. 2012; The juvenile Batten disease protein, CLN3, and its role in regulating anterograde and retrograde post-Golgi trafficking. Clin Lipidol. 7 :79–91. [PubMed: 22545070]

Cotman SL, et al. 2002; Cln3(Deltaex7/8) knock-in mice with the common JNCL mutation exhibit progressive neurologic disease that begins before birth. Hum Mol Genet. 11 :2709–2721. [PubMed: 12374761]

Dargan DJ, Subak-Sharpe JH. 1986; The antiviral activity against herpes simplex virus of the triterpenoid compounds carbenoxolone sodium and cicloxolone sodium. J Antimicrob Chemother. 18 (Suppl B) :185–200.

Davidson JS, Baumgarten IM. 1988; Glycyrrhetinic acid derivatives: a novel class of inhibitors of gap-junctional intercellular communication. Structure-activity relationships. J Pharmacol Exp Ther. 246 :1104–1107. [PubMed: 3418512]

Eliason SL, et al. 2007; A knock-in reporter model of Batten disease. J Neurosci. 27 :9826–9834. [PubMed: 17855597]

Fossale E, et al. 2004; Membrane trafficking and mitochondrial abnormalities precede subunit c deposition in a cerebellar cell model of juvenile neuronal ceroid lipofuscinosis. BMC Neurosci. 5 :57. [PubMed: 15588329]

Geback T, et al. 2009; TScratch: a novel and simple software tool for automated analysis of monolayer wound healing assays. BioTechniques. 46 :265–274. [PubMed: 19450233]

Golabek AA, et al. 2000; CLN3 protein regulates lysosomal pH and alters intracellular processing of Alzheimer's amyloid-beta protein precursor and cathepsin D in human cells. Mol Genet Metab. 70 :203–213. [PubMed: 10924275]

Goldberg GS, et al. 1996; Evidence that disruption of connexon particle arrangements in gap junction plaques is associated with inhibition of gap junctional communication by a glycyrrhetinic acid derivative. Exp Cell Res. 222 :48–53. [PubMed: 8549672]

Hayes MJ, et al. 1977; Changes in the plasma clearance and protein binding of car-benoxolone with age, and their possible relationship with adverse drug effects. Gut. 18 :1054–1058. [PubMed: 606633]

Holopainen JM, et al. 2001; Elevated lysosomal pH in neuronal ceroid lipofuscinoses (NCLs). Eur J Biochem. 268 :5851–5856. [PubMed: 11722572]

Iveson P, et al. 1971; The metabolism of carbenoxolone in the rat. Xenobiotica. 1 :79–95. [PubMed: 5163178]

Kama R, et al. 2011; The yeast Batten disease orthologue Btn1 controls endosome-Golgi retrograde transport via SNARE assembly. J Cell Biol. 195 :203–215. [PubMed: 21987636]

Kenworthy AK. 2007; Fluorescence recovery after photobleaching studies of lipid rafts. Methods Mol Biol. 398 :179–192. [PubMed: 18214381]

Kozler P, Pokorny J. 2003; Altered blood-brain barrier permeability and its effect on the distribution of Evans blue and sodium fluorescein in the rat brain applied by intracarotid injection. Physiol Res. 52 :607–614. [PubMed: 14535837]

Kumari S, Mayor S. 2008; ARF1 is directly involved in dynamin-independent endocytosis. Nat Cell Biol. 10 :30–41. [PubMed: 18084285]

Lamb J, et al. 2006; The connectivity map: using gene-expression signatures to connect small molecules, genes, and disease. Science. 313 :1929–1935. [PubMed: 17008526]

Leshchenko Y, et al. 2006; Carbenoxolone does not cross the blood brain barrier: an HPLC study. BMC Neurosci. 7 :3. [PubMed: 16405728]

Lim MJ, et al. 2007; IgG entry and deposition are components of the neuroimmune response in Batten disease. Neurobiol Dis. 25 :239–251. [PubMed: 17070688]

Liu X, et al. 2010; Gap junctions/hemichannels modulate interkinetic nuclear migration in the forebrain precursors. J Neurosci. 30 :4197–4209. [PubMed: 20335455]

Luiro K, et al. 2001; CLN3 protein is targeted to neuronal synapses but excluded from synaptic vesicles: new clues to Batten disease. Hum Mol Genet. 10 :2123–2131. [PubMed: 11590129]

Luiro K, et al. 2004; Interconnections of CLN3, Hook1 and Rab proteins link Batten disease to defects in the endocytic pathway. Hum Mol Genet. 13 :3017–3027. [PubMed: 15471887]

Monder C, et al. 1989; Licorice inhibits corticosteroid 11 beta-dehydrogenase of rat kidney and liver: in vivo and in vitro studies. Endocrinology. 125 :1046–1053. [PubMed: 2752963]

Metcalf DJ, et al. 2008; Loss of the Batten disease gene CLN3 prevents exit from the TGN of the mannose 6-phosphate receptor. Traffic. 9 :1905–1914. [PubMed: 18817525]

Mole SE, et al. 2005; Correlations between genotype, ultrastructural morphology and clinical phenotype in the neuronal ceroid lipofuscinoses. Neurogenetics. 6 :107–126. [PubMed: 15965709]

Nagayama S, et al. 2001; Carbenoxolone, a new inducer of heat shock protein 70. Life Sci. 69 :2867–2873. [PubMed: 11720090]

Narayan SB, et al. 2006; CLN3P, the Batten's disease protein, is a novel palmitoyl-protein Delta-9 desaturase. Ann Neurol. 60 :570–577. [PubMed: 17036287]

Nevins AK, Thurmond DC. 2006; Caveolin-1 functions as a novel Cdc42 guanine nucleotide dissociation inhibitor in pancreatic beta-cells. J Biol Chem. 281 :18961–18972. [PubMed: 16714282]

Parviainen L, et al. 2017; Glial cells are functionally impaired in juvenile neuronal ceroid lipofuscinosis and detrimental to neurons. Acta Neuropathol Commun. 5 :74. [PubMed: 29041969]

Pearce DA, Sherman F. 1998; A yeast model for the study of Batten disease. Proc Natl Acad Sci U S A. 95 :6915–6918. [PubMed: 9618513]

Pearce DA, et al. 1999; Action of BTN1, the yeast orthologue of the gene mutated in Batten disease. Nat Genet. 22 :55–58. [PubMed: 10319861]

Phillips SN, et al. 2005; CLN3, the protein associated with batten disease: structure, function and localization. J Neurosci Res. 79 :573–583. [PubMed: 15657902]

Porta R, et al. 1986; Gastroprotection and lysosomal membrane stabilization by sulglicotide. Arzneimittelforschung. 36 :1079–1082. [PubMed: 3768076]

Reid JM, O'Neil RG. 2000; Osmomechanical regulation of membrane Trafficking in polarized cells. Biochem Biophys Res Commun. 271 :429–434. [PubMed: 10799314]

Rhee SD, et al. 2012; Carbenoxolone prevents the development of fatty liver in C57BL/6-Lep ob/ob mice via the inhibition of sterol regulatory element binding protein-1c activity and apoptosis. Eur J Pharmacol. 691 :9–18. [PubMed: 22742899]

Rojas R, et al. 2001; Cdc42-dependent modulation of tight junctions and membrane protein Traffic in polarized Madin-Darby canine kidney cells. Mol Biol Cell. 12 :2257–2274. [PubMed: 11514615]

Stein CS, et al. 2010; Osmoregulation of ceroid neuronal lipofuscinosis type 3 in the renal medulla. Am J Physiol Cell Physiol. 298 :C1388–400. [PubMed: 20219947]

Sagare AP, et al. 2013; Neurovascular defects and faulty amyloid-beta vascular clearance in Alzheimer's disease. J Alzheimers Dis. 33 (Suppl 1) :S87–100. [PubMed: 22751174]

Schubert AL, et al. 2002; Connexin family members target to lipid raft domains and interact with caveolin-1. Biochemistry. 41 :5754–5764. [PubMed: 11980479]

Schultz ML, et al. 2014; CLN3 deficient cells display defects in the ARF1-Cdc42 pathway and actin-dependent events. PLoS One. 9 :e96647. [PubMed: 24792215]

Symons AM, Parke DV. 1980; The effects of sodium carbenoxolone on the stability of cellular membranes. Scand J Gastroenterol Suppl. 65 :3–10. [PubMed: 6937938]

Symons AM, et al. 1978; The effect of sodium carbenoxolone on lysosomal enzyme release. Biochem Pharmacol. 27 :2461–2463. [PubMed: 728198]

Tabuchi M, et al. 2012; The blood-brain barrier permeability of 18beta-glycyrrhetinic acid, a major metabolite of glycyrrhizin in Glycyrrhiza root, a constituent of the traditional Japanese medicine yokukansan. Cell Mol Neurobiol. 32 :1139–1146. [PubMed: 22488528]

Takeuchi H, et al. 2011; Blockade of gap junction hemichannel suppresses disease progression in mouse models of amyotrophic lateral sclerosis and Alzheimer's disease. PLoS One. 6 :e21108. [PubMed: 21712989]

Tecedor L, et al. 2013; CLN3 loss disturbs membrane microdomain properties and protein transport in brain endothelial cells. J Neurosci. 33 :18065–18079. [PubMed: 24227717]

Tovar KR, et al. 2009; Direct actions of carbenoxolone on synaptic transmission and neuronal membrane properties. J Neurophysiol. 102 :974–978. [PubMed: 19535488]

Vidal-Donet JM, et al. 2013; Alterations in ROS activity and lysosomal pH account for distinct patterns of macroautophagy in LINCL and JNCL fibroblasts. PLoS One. 8 :e55526. [PubMed: 23408996]

Williams RE, Mole SE. 2012; New nomenclature and classification scheme for the neuronal ceroid lipofuscinoses. Neurology. 79 :183–191. [PubMed: 22778232]

Xiang J, et al. 2016; Mechanisms underlying astrocyte end-feet swelling in stroke. Acta Neurochir Suppl. 121 :19–22. [PubMed: 26463917]

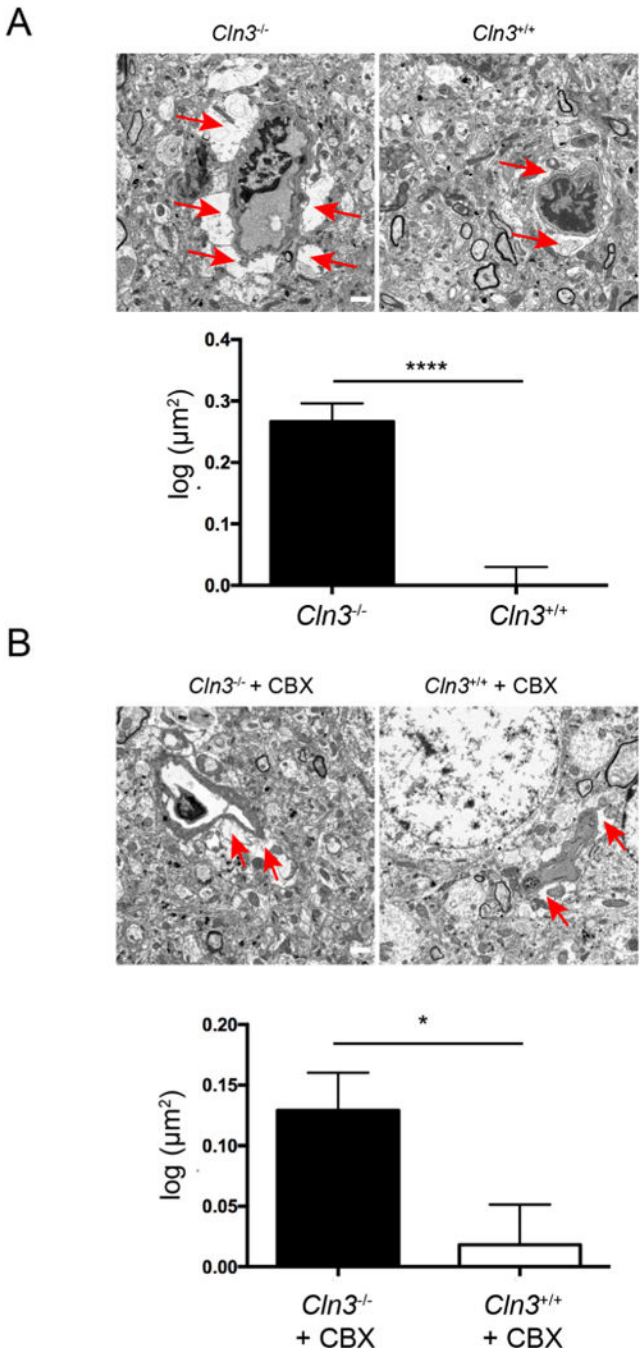

Fig. 1.

Astrocyte endfeet in *Cln3*$^{-/-}$ mice are enlarged. **A**, Astrocytic endfeet in the somatosensory cortex from brain sections harvested from *Cln3*$^{+/+}$ or *Cln3*$^{-/-}$ mice. **B** Astrocyte endfeet in *Cln3*$^{-/-}$ mice can be corrected by CBX treatment. CBX was administered for two weeks by oral gavage and brain sections harvested and evaluated by TEM. For both (A) and (B) the red arrows indicate astrocyte endfeet. Scale bar 1 µm. Astrocytic endfeet area was quantified with ImageJ, n = 342, 327, 436, 398 for *Cln3*$^{-/-}$, *Cln3*$^{+/+}$, *Cln3*$^{-/-}$ + CBX, and *Cln3*$^{+/+}$ + CBX respectively. Results were transformed to normal distribution by log normal function,

and evaluated by *t*-test. *, $p < 0.05$, ****, $p < 0.0001$. Bars show mean ± s.e.m. (For interpretation of the references to colour in this figure legend, the reader is referred to the web version of this article.)

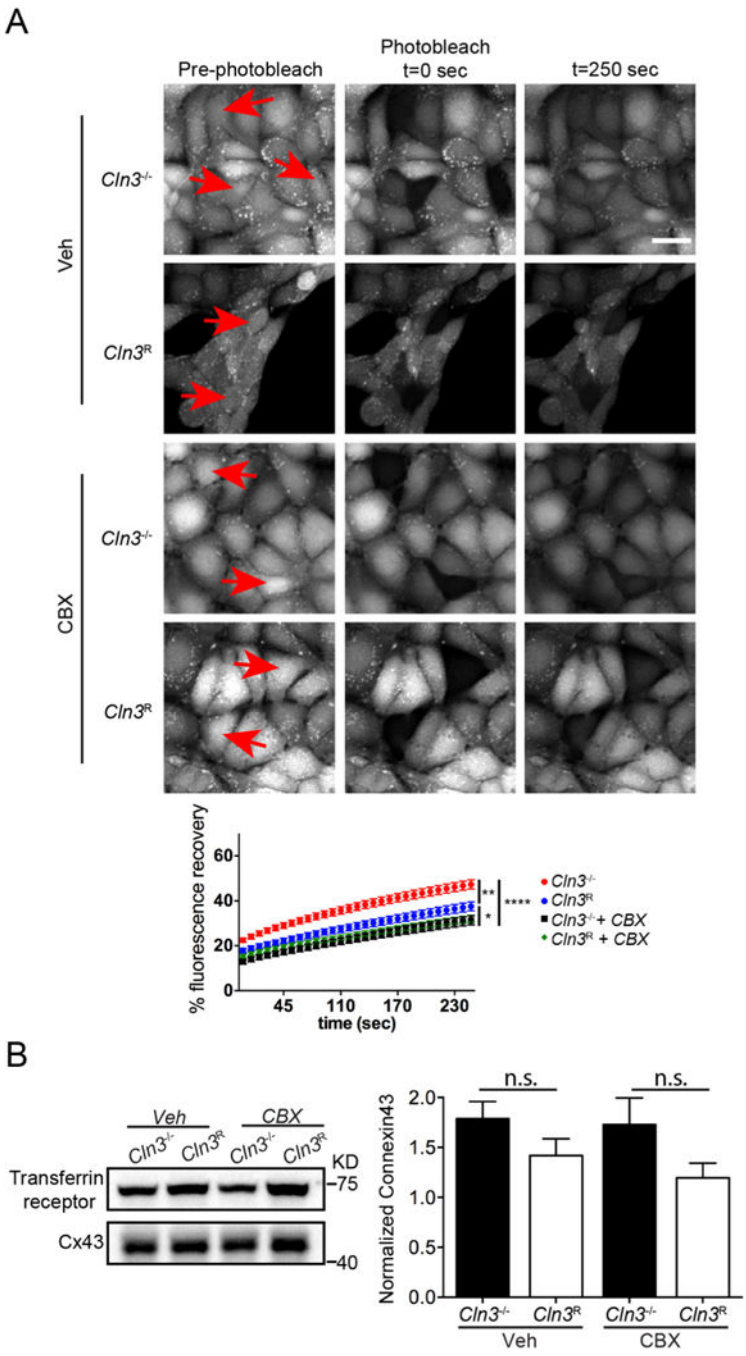

Fig. 2.

CBX corrects GAP junction communication in MBECs. **A**, After calcium-AM was loaded into cells, whole cell FRAP analysis was used to investigate GAP junction communication in *Cln3*^{R} *and Cln3*$^{-/-}$ MBECs. Cells were treated for 2 h with vehicle or 25 μM CBX. ImageJ was used to quantify FRAP over time. Scale bar 20 μm. Data show mean ± s.e.m. from n = 76, 42, 52, 53 *Cln3*$^{-/-}$, *Cln3*^{R}, *Cln3*$^{-/-}$ + CBX, *Cln3*^{R} + CBX cells respectively. Statistical significance was determined by one-way ANOVA with Tukey's multiple comparison test. Relative to *Cln3*^{R}, *Cln3*$^{-/-}$ MBECs had significantly more

calcium-AM recovery at all-time points. * $p < 0.05$, ** $p < 0.01$, **** $p < 0.0001$. **B**, Plasma membrane enriched fractions were analyzed by western blot for Connexin 43 levels. Bars show mean ± s.e.m. of six independent experiments. Analysis with Kruskal-Wallis test showed no significant differences among experimental groups.

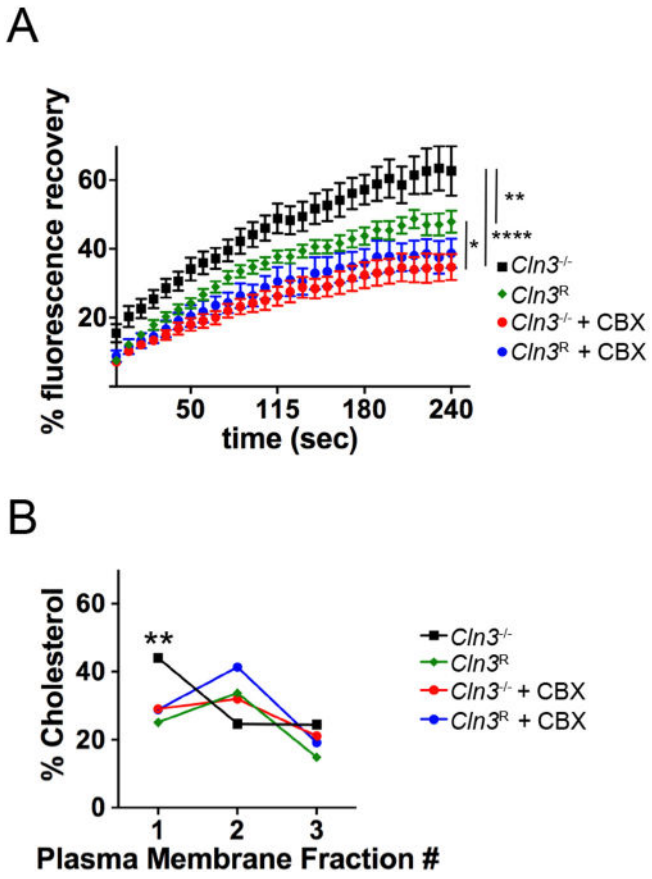

Fig. 3.

CBX treatment repairs membrane fluidity in *Cln3*$^{-/-}$ MBECs. **A**, MBECs were treated with CBX (25 μM) or vehicle for 2 h. The plasma membrane was labeled with Alexa-488-CTB and FRAP was performed using a live cell confocal microscope. ImageJ was used to quantify intensity on images collected over 300 s. Statistical significance was determined by one-way ANOVA with Tukey's multiple comparison test. Relative to *Cln3*^{R}, *Cln3*$^{-/-}$ MBECs had significantly more Alexa-488-CTB recovery at all-time points. * $p < 0.05$, ** $p < 0.01$, **** $p < 0.0001$. **B**, Lipid microdomains were enriched by cell fractionation and the amplex red assay used to quantify cholesterol levels in each fraction. Data are from three independent experiments. Statistical significance was determined by two-way ANOVA with Tukey's multiple comparison test. ** $p < 0.01$. Expanded data in Fig. S1. (For interpretation of the references to colour in this figure legend, the reader is referred to the web version of this article.)

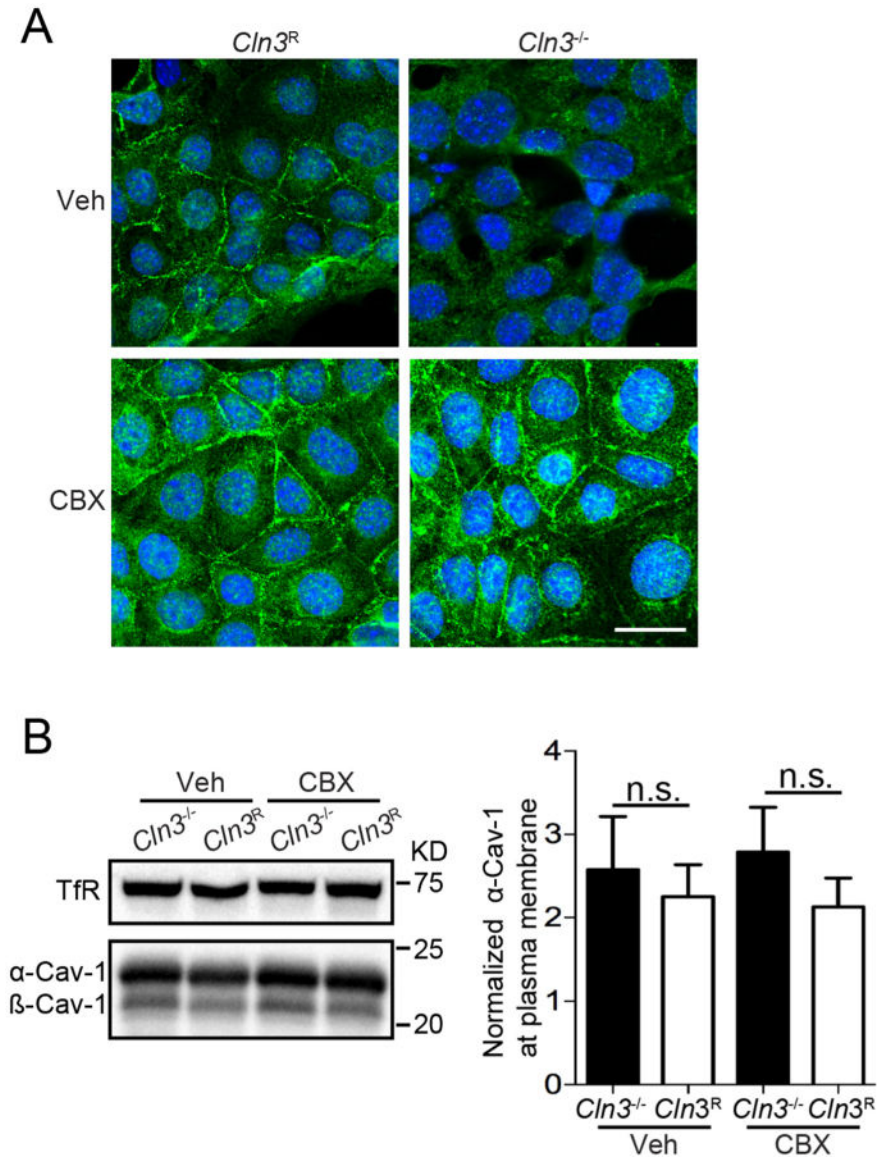

Fig. 4.

CBX restores Cav-1 subcellular localization in *Cln3*$^{-/-}$ MBECs. **A**, MBECs were treated with CBX (25 μM) or vehicle for 2 h, fixed, and Cav-1 intracellular distribution evaluated using immunocytochemistry and confocal microscopy. Photomicrographs are representative of 3 independent experiments. Scale bar = 20 μm.**B**, Western blotting of plasma membrane enriched fractions for Cav-1 levels and quantification. Data are from six independent experiments. Bars show mean ± s.e.m., No statistical differences were found by one-way ANOVA.

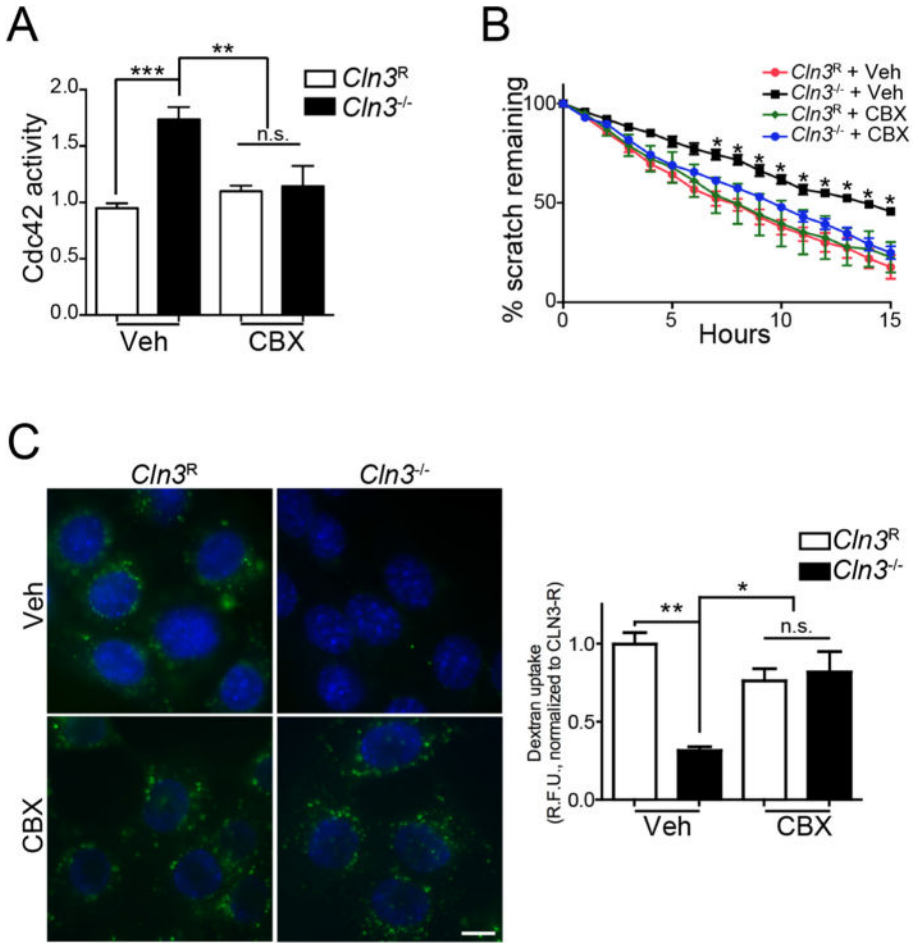

Fig. 5.

Correction of Cdc42-dependent defects in *Cln3*$^{-/-}$ MBECs with CBX. **A**, MBECs were treated for 2 h with CBX (50 μM) or vehicle and Cdc42-GTP levels were measured. Data are mean ± SEM of 5 independent experiments, one-way ANOVA with Tukey's multiple comparison correction. **B**, MBECs were grown to confluence, a scratch wound made, and CBX (3.5 μM) or vehicle added to cells. Cell migration was imaged overnight and quantified by T-Scratch software. Data are mean ± s.e.m. from 4 independent experiments evaluated by one-way ANOVA with Tukey's post-hoc correction. **C**, MBECs were treated with CBX (25 μM) or vehicle and endocytic uptake assessed by A488-Dextran uptake (*green*). Hoechst 33342 was used to label nuclei (*blue*). Non-internalized extracellular dextran was quenched by Red-40 and epifluorescent images were quantified by ImageJ. Data are mean ± s.e.m. from ~70 cells from 3 independent experiments, and evaluated one-way ANOVA with Tukey's post-hoc. For all panels *, $p < 0.05$, **, $p < 0.01$, ***, $p < 0.001$, n.s. = not significant. (For interpretation of the references to colour in this figure legend, the reader is referred to the web version of this article.)

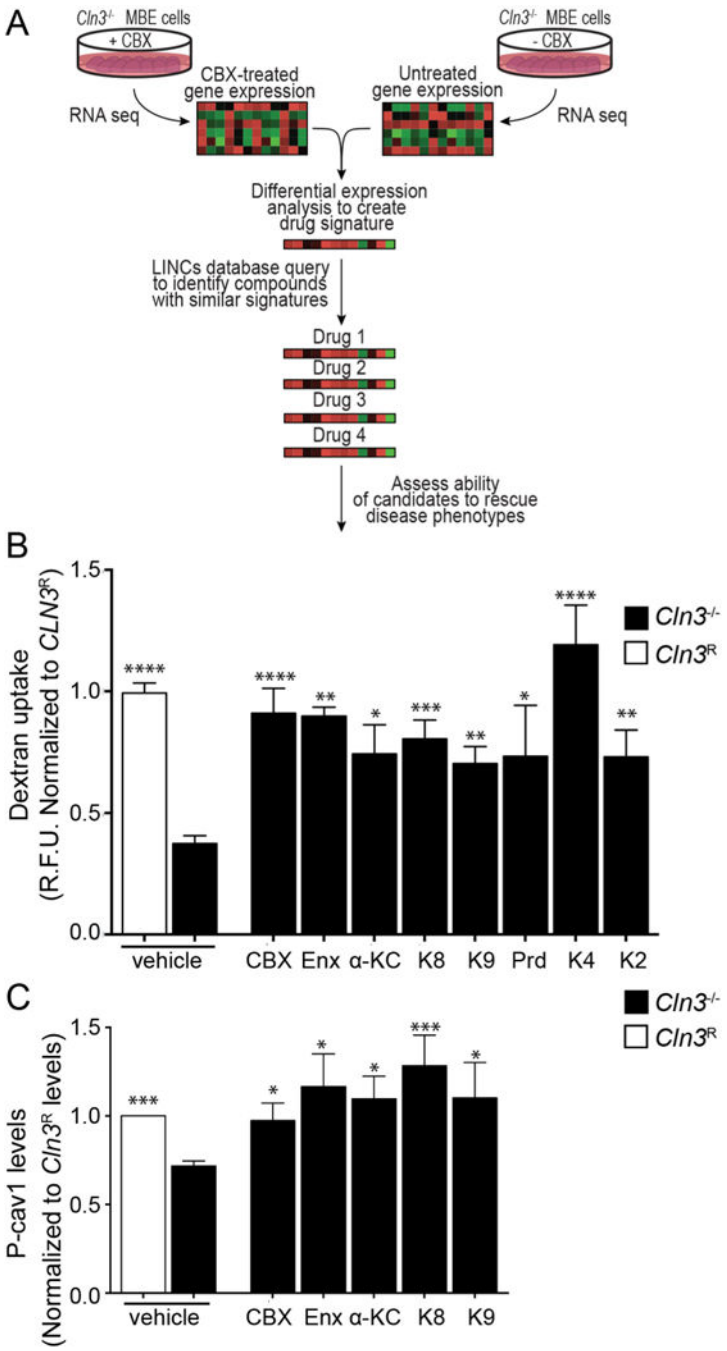

Fig. 6.

Multidrug screening. **A**, LINCs strategy to identify compounds with signatures similar to CBX. **B**, Fluid-phase endocytosis was analyzed by Alexa 488-dextran uptake (as in Fig. 5C). Data are mean ± s.e.m. from 4 to 8 independent experiments for each small molecule, one-way ANOVA with Holm-Sidak's multiple comparisons post-hoc for analyzing differences of vehicle treated *Cln3*^{R} MBECs with respect to all other groups. **C**, Phosphorylated Cav-1(P-cav1) levels in *Cln3*^{R} and *Cln3*$^{-/-}$ MBECs after small molecule treatment. Data represent mean ± s.e.m. from six independent experiments, non-parametric Mann-Whitney

test with Bonferroni's multiple comparison correction for vehicle treated *Cln3*$^{-/-}$ MBECs with respect to all other groups. * $p < 0.05$, ** $p < 0.01$, *** $p < 0.001$, **** $p < 0.0001$. Carbenoxolone (CBX), Enoxolone (Enx), Prednisolone (Prd), α-ketocholesterol (α-KC), BRD-K95814727 (K8), BRD-K30446755 (K4), BRD-K33258928 (K2), BRD-K95985487 (K9).

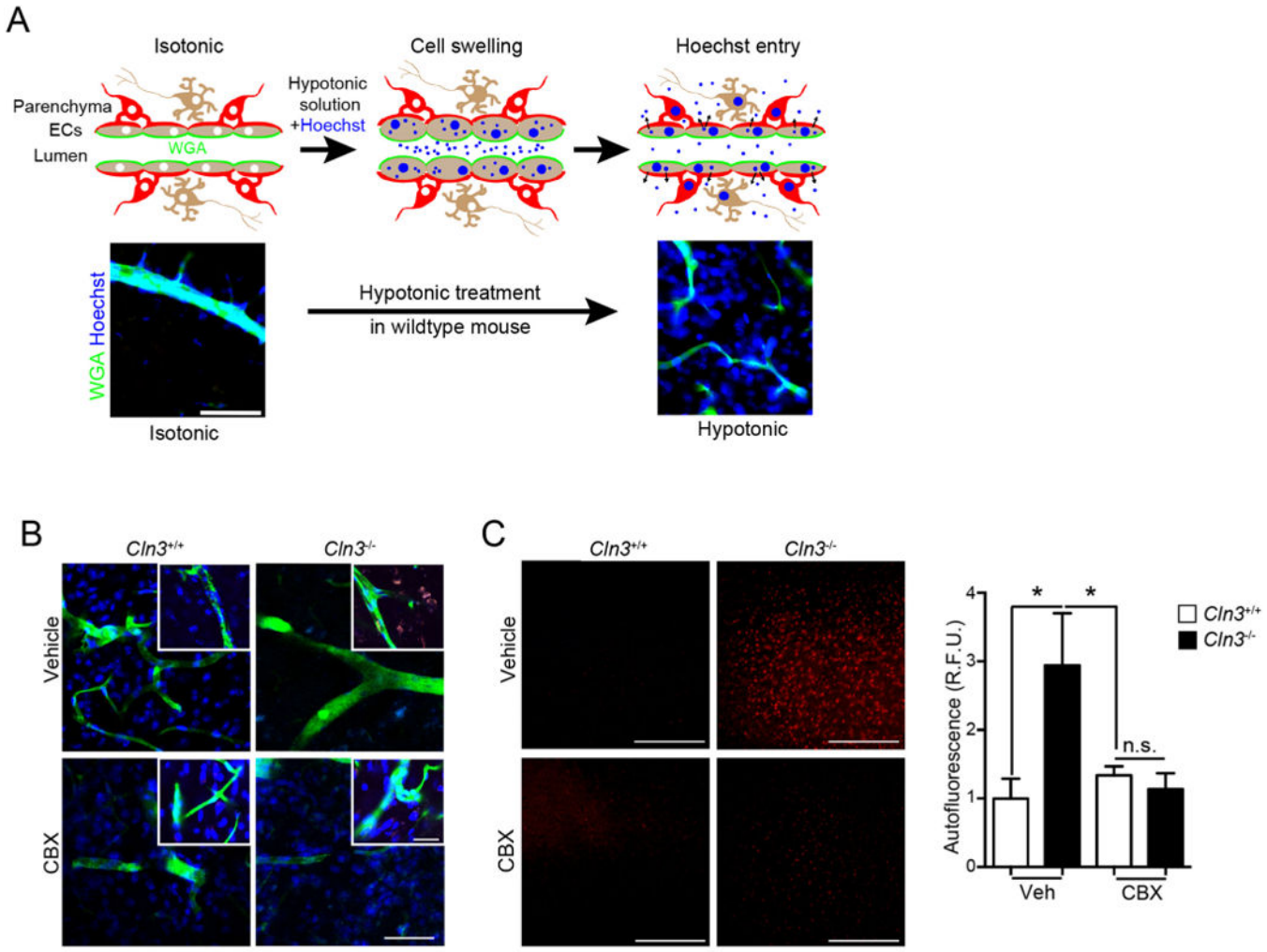

Fig. 7.

CBX corrects regulated volume defects and reduces *Cln3*$^{-/-}$ autofluorescent inclusions *in vivo*. **A**, (Top) Schematic representing Hoechst entry into the brain during hypotonic treatment. (Bottom) *Cln3*$^{+/-}$ mice exposed to isotonic or hypotonic treatments. Animals were anesthetized and wheat germ agglutinin (WGA) (*green*) infused intravascularly to label endothelial cells followed by infusion of Hoechst dye (*blue*) in a hypotonic solution, then saline infusion, followed by fixation, sectioning and imaging. The Hoechst signal outside the WGA-labeled vascular is indicative of regulated volume decrease and dye extravasation after hypotonicity exposure. Scale bar = 100 μm. **B**, *Cln3*$^{+/+}$ or *Cln3*$^{-/-}$ mice were treated daily with vehicle or 20 mg/kg CBX for two weeks. After anesthetization, mice were perfused as in (**A**). Brain slices (50 μm) were imaged by confocal microscopy and show that CBX permits Hoechst dye extravasation in *Cln3*$^{-/-}$ mice brain. Images are representative of 5 mice per group performed on different days. Scale bar = 50 μm. **C**, Thin sections from fixed brains were imaged under low magnification in the red channel to detect autofluorescence. Scale bar = 200 μm. Cortical images (4 images/animal; 4 mice/group) were taken and fluorescence intensity averaged using ImageJ. Data are mean ± s.e.m., Kruska-Wallis test with Tukey's multiple comparisons post-hoc, *, $p < 0.05$. Scale bar is 200 μm. (For

interpretation of the references to colour in this figure legend, the reader is referred to the web version of this article.)